nature photonics

ARTICLES

https://doi.org/10.1038/s41566-022-00985-1

Quantum-size-tuned heterostructures enable efficient and stable inverted perovskite solar cells

Hao Chen[1,2,7], Sam Teale[1,7], Bin Chen[1,7], Yi Hou[1,6,7], Luke Grater[1], Tong Zhu[1], Koen Bertens[1], So Min Park[1,3], Harindi R. Atapattu[3], Yajun Gao[4], Mingyang Wei[1], Andrew K. Johnston[1], Qilin Zhou[2], Kaimin Xu[2], Danni Yu[2], Congcong Han[2], Teng Cui[5], Eui Hyuk Jung[1], Chun Zhou[1], Wenjia Zhou[2], Andrew H. Proppe[1], Sjoerd Hoogland[1], Frédéric Laquai[4], Tobin Filleter[5], Kenneth R. Graham[3], Zhijun Ning[2]✉ and Edward H. Sargent[1]✉

The energy landscape of reduced-dimensional perovskites (RDPs) can be tailored by adjusting their layer width (*n*). Recently, two/three-dimensional (2D/3D) heterostructures containing $n=1$ and 2 RDPs have produced perovskite solar cells (PSCs) with >25% power conversion efficiency (PCE). Unfortunately, this method does not translate to inverted PSCs due to electron blocking at the 2D/3D interface. Here we report a method to increase the layer width of RDPs in 2D/3D heterostructures to address this problem. We discover that bulkier organics form 2D heterostructures more slowly, resulting in wider RDPs; and that small modifications to ligand design induce preferential growth of $n\geq3$ RDPs. Leveraging these insights, we developed efficient inverted PSCs (with a certified quasi-steady-state PCE of 23.91%). Unencapsulated devices operate at room temperature and around 50% relative humidity for over 1,000 h without loss of PCE; and, when subjected to ISOS-L3 accelerated ageing, encapsulated devices retain 92% of initial PCE after 500 h.

Reduced-dimensional perovskites are perovskite quantum well (QW) layers confined between large organic ligands. The number of stacked lead (Pb) octahedra between the organic spacers determines the width of the RDP layer: $n=1$, 2, 3 and so on (Fig. 1a). Changing the RDP layer width (n) within bulk RDP films alters the energy landscape of the resulting material, hence narrow RDP films ($n\leq5$) produce excellent light-emitting diodes (LEDs) and luminescent solar concentrators[1,2]. Although films containing wider RDPs ($n\geq10$) have been used to produce highly stable PSCs, these devices suffer from an inferior performance due to poor carrier mobility[3,4]. More recently, record-performing PSCs have used a 2D/3D heterostructure, fabricated via spin coating RDP (or 2D) ligands onto the surface of a 3D perovskite[5–12]. A comparison of PSC efficiency/stability from recent reports is shown in Supplementary Fig. 1 and demonstrates that all of the most efficient devices reported have used this structure. Studies have revealed that this heterostructure consists of a thin layer of $n=1$ and/or $n=2$ RDPs atop a bulk 3D perovskite[13–16], which increases performance via passivation and increased electron blocking[17,18]. Electron blocking is beneficial for devices built in the negative–intrinsic–positive (NIP) architecture, in which the 2D-treated perovskite surface is coated with a hole transport layer (HTL); however, when used in the generally more stable[19–22] inverted (that is, positive–intrinsic–negative, or PIN) structure, this strategy achieves mixed results. Chen et al. found that a 2D treatment applied to inverted cells improved the open-circuit voltage (V_{OC}) but reduced the fill factor (FF)[23], and Bai et al. found that introducing a small amount of 2D ligand into the antisolvent improved the device performance, opening the door to further study of the width of RDPs and indeed their presence[24]. On the other hand, Park et al., La-Placa et al. and Zhao et al. all found that using a 2D layer in a PIN device reduced the PCE due to a lower current and fill factor[25–27]. We speculated that reducing the confinement in the 2D layer could reduce electron blocking and produce inverted PSCs with an exceptional performance.

A quasi-2D surface treatment

Using ultraviolet photoelectron spectroscopy (UPS) and absorption spectroscopy, we estimated the band alignment of RDP films of differing QW widths ($n=1$–4; Fig. 1b) and compared them with the bulk 3D perovskite $Cs_{0.05}MA_{0.1}FA_{0.85}PbI_3$ (MA, methylammonium; FA, formamidinium). Consistent with earlier reports, we found little dependence between the valence band maximum (VBM) and n (RDP width)[18,28,29]. Instead, quantum confinement upshifts the conduction band minimum (CBM), which induces electron blocking in the devices. We confirmed this detrimental effect by comparing NIP and PIN PSCs treated using standard 2D treatments (Supplementary Text 1). Encouragingly, simulations using the solar cell simulation tool SCAPS-1D[30] suggested that, due to their deeper CBM, a capping layer of $n\geq3$ RDPs would be beneficial for PIN solar cell performance via surface passivation with reduced resistance to carrier transport (Supplementary Text 2).

In bulk RDP films, the average layer thickness is modulated by changing the ratio of the 2D ligands to the 3D perovskite precursors in solution[1,4]. We explored several options to reproduce this

[1]The Edward S. Rogers Department of Electrical and Computer Engineering, University of Toronto, Toronto, Ontario, Canada. [2]School of Physical Science and Technology, ShanghaiTech University, Shanghai, China. [3]Department of Chemistry, University of Kentucky, Lexington, KY, USA. [4]KAUST Solar Center, Physical Sciences and Engineering Division (PSE), Materials Science and Engineering Program (MSE), King Abdullah University of Science and Technology (KAUST), Thuwal, Kingdom of Saudi Arabia. [5]Department of Mechanical and Industrial Engineering, University of Toronto, Toronto, Ontario, Canada. [6]Present address: Department of Chemical and Biomolecular Engineering, National University of Singapore, Singapore, Singapore. [7]These authors contributed equally: Hao Chen, Sam Teale, Bin Chen, Yi Hou. ✉e-mail: ningzhj@shanghaitech.edu.cn; ted.sargent@utoronto.ca

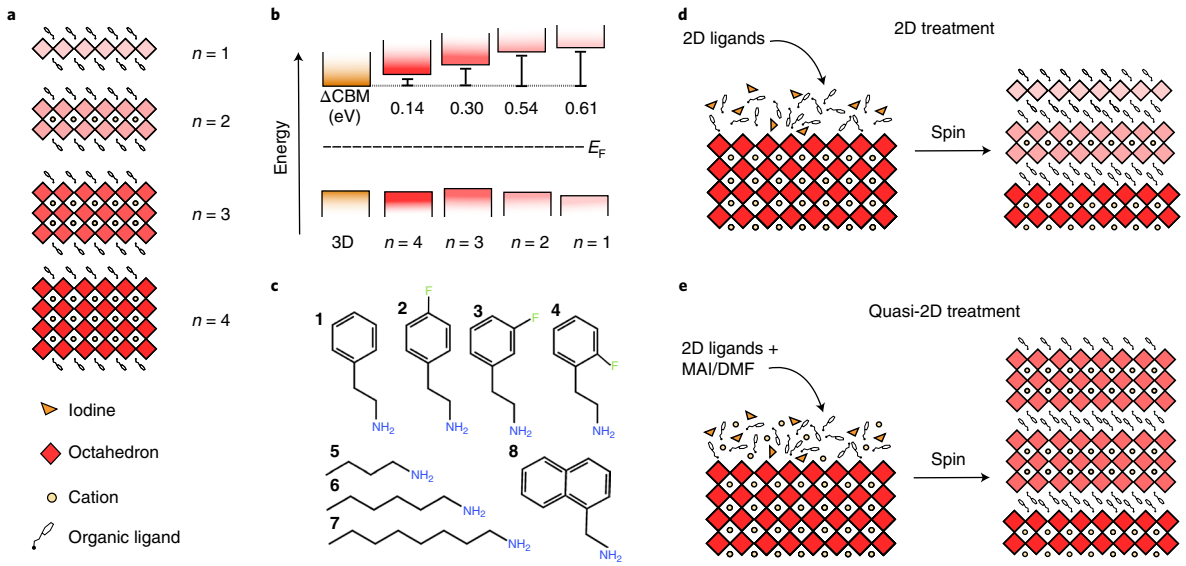

Fig. 1 | Quasi-2D treatment and its effect on RDP distribution. a, Schematic of $n=1$, 2, 3 and 4 RDPs. **b**, Band alignment of 3D and RDP films with increasing confinement calculated from UPS and the optical bandgap of quasi-2D perovskite films. **c**, The eight ligands used in the study: **1**, phenethylammonium; **2**, 4-fluoro-phenethylammonium; **3**, 3-fluoro-phenethylammonium; **4**, 2-fluoro-phenethylammonium; **5**, butylammonium; **6**, hexylammonium; **7**, octylammonium; and **8**, 1-naphthylmethylammonium. **d**,**e**, Schematics of the standard 2D treatment (**d**) and the quasi-2D treatment (**e**) producing $n \leq 2$ RDPs and $n \geq 2$ RDPs, respectively.

for a 2D post-treatment (Supplementary Text 3). Our most distinctive results came from introducing a small amount of dimethylformamide (DMF) (at 1:200 by volume in isopropanol (IPA)) and methylammonium iodide (MAI) (1:2 by weight) to the 2D ligands in solution. We posit that MAI is needed to reduce the ratio of the 2D ligand to the A-site cation and that DMF introduces Pb directly from the 3D perovskite surface (Supplementary Fig. 9). Using this strategy, we were able to produce 2D perovskite capping layers containing $n \geq 3$ RDP layers (Fig. 1e). For convenience, we henceforth refer to our altered 2D ligand treatment as a quasi-2D treatment.

Notably, Zhou et al. demonstrated that adding MAI and DMF to a phenethylammonium iodide (PEAI) surface treatment improves the performance of PIN solar cells[31]. This earlier study is limited in scope, however, discussing only the effect of DMF on the penetration depth of the 2D treatment. Using time-of-flight secondary-ion mass spectrometry, we estimated the penetration depth of phenethylammonium (PEA) from solutions using different DMF concentrations (Supplementary Fig. 11) and found no correlation in our sample size (from 1:200 to 1:50 DMF:IPA by volume). We instead expect that the origin of improved performance is the production of wider RDPs at the interface between the 3D perovskite and the electron transporting layer (ETL). Considering this new observation, we sought a treatment that would optimize this effect.

Characterizing the quantum well width in 2D/3D heterojunctions

A strong dependence between QW width and bandgap exists in 2D perovskites[32,33]. Hence, ultrafast transient absorption (TA) spectroscopy is able to accurately identify the distribution of different 2D species in perovskite films[34–36]. We first acquired the TA spectra of 2D- and quasi-2D-treated films using the most common 2D perovskite ligands: butylammonium (BTA) (Fig. 2a,d) and PEA (Fig. 2b,e). Although the majority absorption from each film is from the 3D perovskite (780 nm, Supplementary Fig. 12), each film displays bleach peaks in the 500–700 nm range, characteristic of RDPs. Similar to spectra acquired by Niu et al., the standard 2D-treated films display bleach signals from $n=1$ and/or 2 RDPs[36]. Quasi-2D-treated films, however, contain $n \geq 3$ RDPs, with the PEA treatment producing more $n \geq 3$ RDPs than BTA. Grazing incidence wide-angle X-ray scattering (GIWAXS) confirmed that these 2D layers lie horizontal to the substrate (Supplementary Fig. 13), as in other reports[5,13,15]. Recently, it was documented that bulk quasi-2D perovskite films made using fluorinated PEA ligands form different QW structures compared to unfluorinated PEA[35]. To this end, we tested PEA-based ligands with a fluorine at each node (Fig. 1c) and found that this has a dramatic effect on the QW distribution (Supplementary Fig. 16). Mostly notably, we found that using our quasi-2D surface strategy, 3-fluoro-phenethylammonium (3F-PEA) produces a 2D/3D heterojunction containing majority $n=3$ RDP (Fig. 2f). The structures of all 2D ligands mentioned are shown in Fig. 1c.

To better understand why different ligands produce different RDP distributions, we the measured TA spectra in situ while spin coating quasi-2D treatments (Fig. 2g–i). With a pump–probe delay of 1 ps and a time resolution of 0.3 s, we spun films at 1,500 revolutions per minute (r.p.m.) and deposited the 2D treatment dynamically. A reduction in the 3D perovskite absorption is apparent ~2.4 s after solution deposition for all samples. For the BTA treatment, this reduction in 3D bleach is concurrent with the arrival of a strong $n=2$ bleach. For the PEA-based treatments, the 2D signal does not appear until ~1.2 s after the 3D bleach reduction. It has been suggested that bulkier organics intercalate more slowly, which induces them to form wider RDPs[34]. Our results agree, indicating that π–π stacking ligands form wider RDPs due to slower crystallization, which suppresses narrower RDP formation. This is corroborated by films treated using hexylammonium (HA) and octylammonium (OTA) ligands, which demonstrate an increased presence of $n \geq 3$ RDP with increasing ligand length (Supplementary Fig. 14). To investigate the effect of increased π–π stacking, we treated samples with 1-naphthylmethylammonium (Fig. 1c) but found that the quasi-2D treatment substantially reduced the RDP absorption in the TA spectra (Supplementary Fig. 15). We also gained insight into why 3F-PEA forms wider RDPs. Standard PEA produces $n=2$ and 3 simultaneously, whereas 3F-PEA forms $n=3$

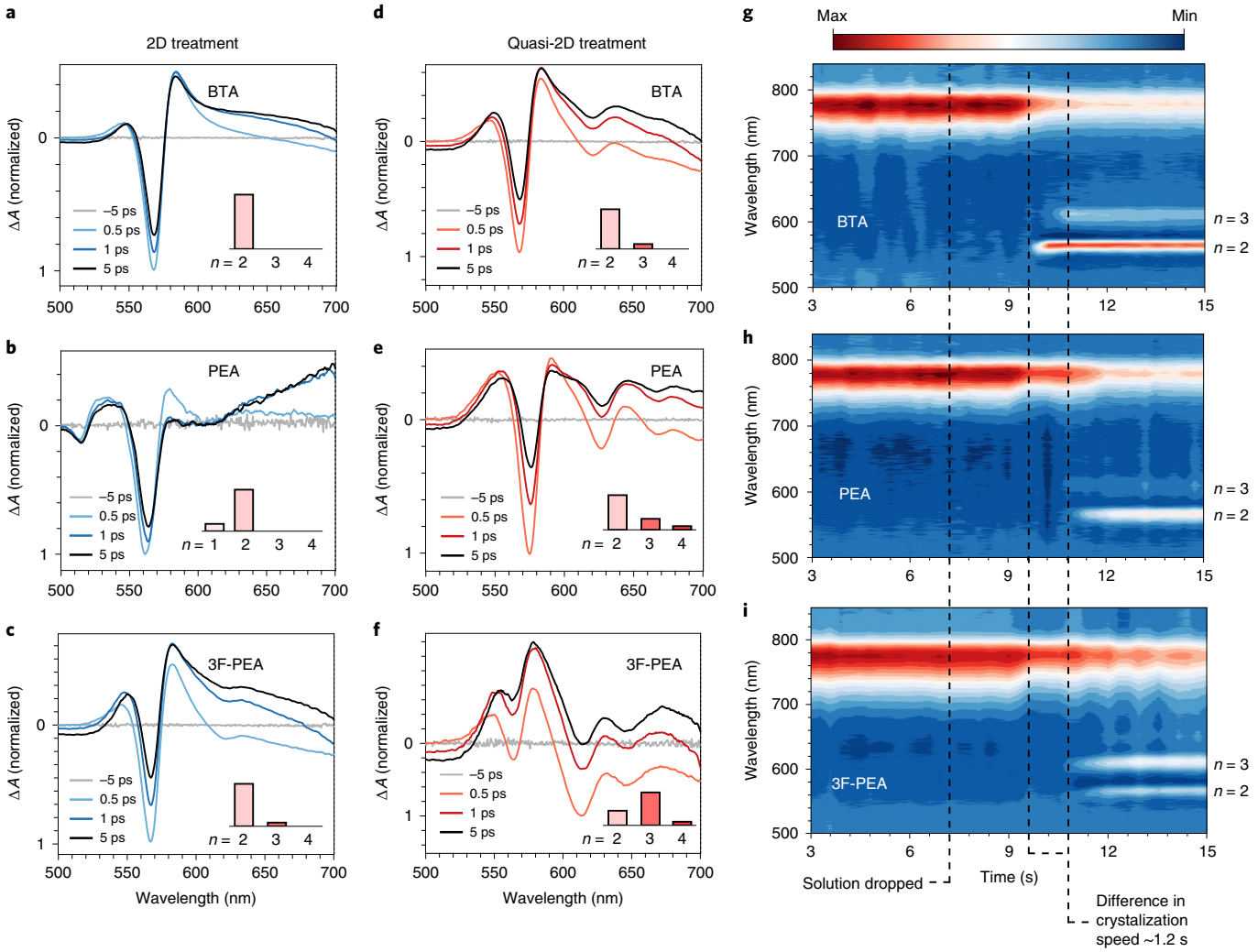

Fig. 2 | Comparison of 2D and quasi-2D treatments using different 2D ligands. a–c, TA spectra of films treated with BTA (**a**), PEA (**b**) and 3F-PEA (**c**) using the standard 2D treatment. **d–f**, TA spectra of films treated with BTA (**d**), PEA (**e**) and 3F-PEA (**f**) using the quasi-2D treatment. The majority absorption in each case is from the 3D perovskite (780 nm) but this has been excluded for clarity. Absorption peaks are assigned in order, and a comparison with single-cation quasi-2D films is shown in Supplementary Table 4. The inset bar in **a–f** represents the relative absorption from each RDP species. **g–h**, Absorption maps from in situ TA spectroscopy obtained during spin coating. $Cs_{0.05}MA_{0.1}FA_{0.85}PbI_3$ 3D perovskite films were spun at 1,500 r.p.m. and a constant 1 ps pump–probe delay time was used. The quasi-2D treatments for BTA (**g**), PEA (**h**) and 3F-PEA (**i**) were all dropped at 7.2 s.

one frame (0.3 s) before the appearance of $n=2$, suggesting that $n=3$ is preferentially formed from the precursor complex.

Density functional theory (DFT) calculations were used to compute the formation energy of $n=1$, 2, 3 and 4 RDPs for each ligand (details in Supplementary Text 5). As previously reported[4], the formation energy of the $n=1$ RDP was found to be the lowest for all ligands; however, this was not supported by our experimental findings or results from other studies[36,37]. Nonetheless, considering that forming single layers of lead iodide (PbI_2) is considerably more energy intensive than larger slabs (Fig. 3a) it seems reasonable that $n=1$ layers are less likely to form, especially when excess cations are available as within the quasi-2D treatment. Hence, we compared the formation energy of $n\geq 2$ RDPs. Generally, we found that formation energy increases with increasing width, however, we also found that bonding different ligands onto 2D perovskite flakes ($FA_{n-1}Pb_nI_{3n-1}$) introduces different types of strain into the system which is released through different distortions of the perovskite (Supplementary Fig. 22). The specific orientation and arrangement of the ligands caused by the fluorine atom in 3F-PEA (structure taken from[35]) introduces larger strain compared to PEA or BTA, manifesting as larger distortions, and therefore larger perovskite flakes are need to fully release the additional strain. As a result, a sweet spot for $n=3$ is found in the formation energy of 3F-PEA (Fig. 3b), which results in the preferential formation of $n=3$ revealed in the TA data. We calculated the formation energies for each of the ligands **1**–**7** in Fig. 1c (Supplementary Fig. 21, Supplementary Text 5), but only 3F-PEA possessed a preference for $n\geq 3$.

Band alignment of 2D/3D heterostructures

We proposed to modulate the n distribution of 2D/3D heterojunctions with the aim of reducing the electron barrier at the perovskite/ETL interface. To verify this, we used surface-sensitive inverse photoelectron spectroscopy (IPES), which directly measures the conduction band of the first few nanometres of film[29,38–41]. Following work from Endres et al.[42] we used gaussian fittings to extract the CBM and found that, as expected, the CBM values of 2D-treated surfaces are upshifted compared with the controls (Fig. 4a–c). Using the quasi-2D treatment the 2D/3D CBM offset is reduced substantially for PEA- and 3F-PEA-treated films relative to their $n=1$ (and/or 2) analogues (0.42–0.14 eV and 0.49–0.08 eV, respectively)

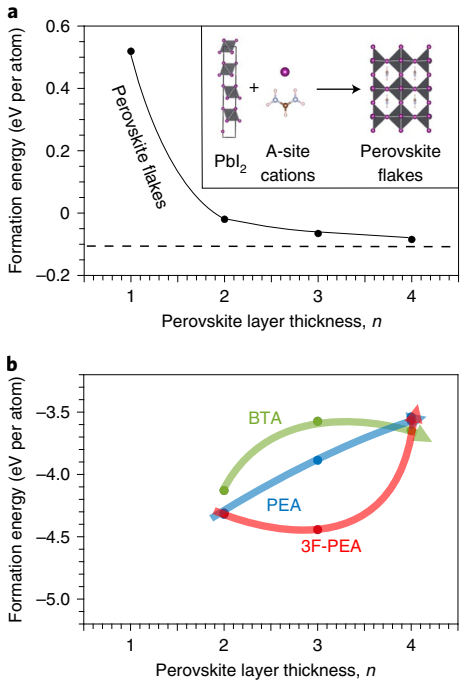

Fig. 3 | Formation of quasi-2D perovskite capping layers from density functional theory. a, The PBE+TS calculated formation energy of perovskite flakes ($(FA)_{n-1}Pb_nI_{3n-1}$, see inset). The formation energy of $FAPbI_3$ is shown as a dashed line. Note that the energy required to form a single-layer (PbI_2) flake ($n=1$ RDP) is much higher than for other layer widths. PBE+TS, Perdew–Burke–Ernzerhof functional with the Tkatchenko–Scheffler dispersion correction. **b**, The formation energy of different RDPs dependent on the layer width n and the ligand (BTA, PEA and 3F-PEA). The same calculations were performed on HA, OTA, 2F-PEA and 4F-PEA and can be found in Supplementary Fig. 21.

but less so for BTA (0.41–0.31 eV). We measured the potential of our film surfaces using Kelvin probe force microscopy (KPFM) and found a similar trend (Supplementary Fig. 17). This complements the results in the previous section which suggest that the quasi-2D treatment using BTA produces fewer $n \geq 3$ RDPs than PEA or 3F-PEA. We also performed surface-sensitive UPS on control, 2D- and quasi-2D-treated films (Supplementary Fig. 18) to produce the schematics in Fig. 4e,f. Similar to the plot in Fig. 1b and several previous reports[18,28,29], altering the RDP width has little effect on the VBM, and reducing confinement simply shifts the conduction band deeper, closer to the 3D perovskite. More details on these UPS and IPES measurements can be found in Supplementary Text 4.

Carrier extraction and photovoltaic performance

To explore the device implications, we investigated the charge transport in BTA-, PEA- and 3F-PEA-treated films using the 2D and quasi-2D treatments. The photoluminescence quantum yield (PLQY) increases after the standard 2D treatment for each ligand (Supplementary Table 6), suggesting a reduced density of non-radiative recombination centres[8]. This effect is enhanced slightly by the quasi-2D treatment, indicating improved passivation. A similar trend is visible in transient photoluminescence (TRPL) spectroscopy results (Fig. 5a and Supplementary Fig. 24), where longer lifetimes are recorded for 2D- and quasi-2D-treated films (a summary of lifetimes is found in Supplementary Table 3). The modestly improved passivation of the quasi-2D treatment may be due to the addition of MAI, which has also been reported to passivate perovskite surfaces[43].

Following the work of Kirchartz et al., we deposited [6,6]-phenyl-C_{61}-butyric acid methyl ester (PCBM) atop the perovskite as an ETL and used the quenched τ_1 lifetimes to compare charge extraction (Fig. 5b)[44]. The quenched τ_1 lifetime of the control film was 4.6 ns. After deposition of 3F-PEA this doubled to 9.2 ns, suggesting that the standard 2D treatment impedes the flow of electrons from the perovskite to the ETL. Using the quasi-2D treatment this was reduced to 4.9 ns, implying a considerably improved extraction compared with the standard 2D treatment. A similar trend is seen using BTA and PEA (Supplementary Fig. 24). For quantitative values we repeated these observations using power-dependent TA (Supplementary Text 6 and Supplementary Table 8) and space-charge-limited current (SCLC) measurements. From the TA data we found that both 2D and quasi-2D treatments reduced the surface recombination velocity (from ~600 $cm\,s^{-1}$ to ~300 $cm\,s^{-1}$). The SCLC measurements show a similar trend (Supplementary Fig. 27) but the overall effect is less obvious as we are examining the entire film and not simply the interfaces.

In PSCs using bulk RDPs, films that contain mixed-dimensional phases have reduced mobility due to charge trapping in the higher n species[3]. To understand why this is not necessarily the case in 2D/3D heterostructure films, we used TA spectroscopy to measure the charge dynamics. Using a 450 nm pump at a low power (5 $\mu J\,cm^{-2}$) to avoid Auger recombination[45], we excited the 2D and 3D layers of 2D- and quasi-2D-treated films. Measuring the $n=2$ bleach decay (~570 nm) using monoexponential fits, we calculated the carrier funnelling rates for both treatments; a summary of the results is shown in Supplementary Fig. 28. For a standard 2D-treated film, there are no peaks present for $n>2$ (Fig. 2a), thus we expect the charges to funnel directly from $n=2$ to the 3D perovskite[1,46], for which we observed a 28.6 ps decay time. When we generate a favourable pathway for electrons by adding a layer of PCBM, we observed a faster decay (7.5 ps). Repeating these measurements with a quasi-2D-treated film, we observed a decay without PCBM of 5.8 ps, suggesting that the charges are funnelled to the now present $n>2$ species[1,46]. However, adding a layer of PCBM resulted in an even faster decay (1.2 ps), indicating that charge trapping does not play a limiting role in charge extraction.

To gauge the effect of the 2D and quasi-2D treatments in full device stacks, we conducted transient photovoltage (Supplementary Fig. 25) and transient photocurrent measurements (Fig. 5c). Following ref. [47], devices were biased with the same white-light intensity to reach near-V_{OC} conditions and were photoexcited with low-power laser pulses to generate small photovoltage perturbations (ΔV, kept to lower than 20 mV). Monoexponential fits were used to estimate the carrier lifetime under V_{OC} and short-circuit current density (J_{SC}) conditions. We observed a slower decay in photovoltage for the quasi-2D-treated films compared with the standard 2D treatment (Supplementary Fig. 25), which is consistent with the TRPL results and indicates a reduction in trap states in the absorber. More importantly, we observed a faster decay in the photocurrent for the quasi-2D-treated films ($\tau_{quasi\text{-}2D}=0.82\,\mu s$ compared with $\tau_{2D}=1.28\,\mu s$ for 3F-PEA-treated films), which suggests a substantial improvement in carrier extraction[48]. In addition, we performed conductive atomic force microscopy (c-AFM) on these films, revealing increased conductivity in quasi-2D-treated films (Supplementary Figs. 31 and 32).

We fabricated devices with an ITO/NiO_x nanoparticles/perovskite/PCBM/BCP/Ag structure using different surface treatments (BTA, PEA, 2F-PEA, 4F-PEA and 3F-PEA; standard 2D and quasi-2D treatments) for statistical analysis (Supplementary Figs. 33–36). In agreement with our finding that increased $n \geq 3$ RDPs result in more efficient charge extraction, 3F-PEA outperformed the PEA- and BTA-treated devices. Improved performance of the quasi-2D-treated over the standard 2D-treated devices is derived mainly from FF and J_{SC} improvements; a typical set of

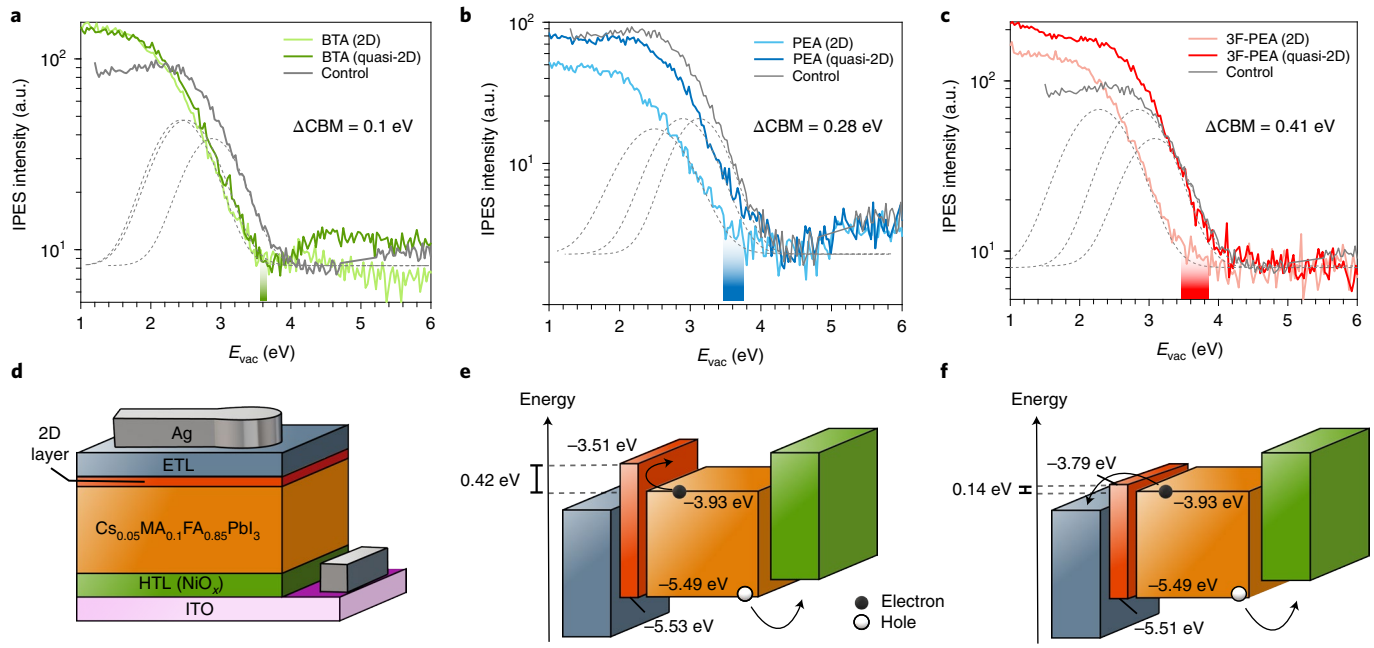

Fig. 4 | Quantifying the conduction band offset of 2D and quasi-2D surface treatments. a–c, IPES spectra of BTA- (**a**), PEA- (**b**) and 3F-PEA-treated (**c**) films using 2D and quasi-2D treatments. The dashed lines represent the gaussians used to fit the data. The shaded region represents the change in conduction band edge. IPES measurements were taken using a bandpass filter of 254 nm (4.88 eV) for the control and PEA-treated films and 280 nm (4.42 eV) for BTA- and 3F-PEA-treated films. E_{vac}, vacuum level. **d**, Cross-section of a typical 2D/3D heterostructure in the PIN configuration. **e**,**f**, The band alignment of the resulting cell using the 2D treatment (**e**) or the quasi-2D treatment (**f**). Values in **e**,**f** were calculated for a PEA treatment using combined UPS and IPES.

current density–voltage (J–V) curves are shown in Fig. 5d along with their figures of merit. To check the reproducibility, we provide statistics for devices fabricated over a one-year period (September 2020 until September 2021) in Supplementary Figs. 37–39. To confirm that improved passivation alone was not the cause of the increased FF, we simulated the effect of reducing only the surface trap density using the SCAPS-1D simulation tool (Supplementary Fig. 40) and found that a 20 mV difference in V_{OC} would correspond to an increase in FF of approximately 0.5% rather than the 2.2% increase manifested.

A quasi-2D-treated device was certified at the National Renewable Energy Laboratory (NREL). The C_{60}/BCP-based device produced a quasi-steady-state certified PCE for inverted PSCs of 23.91% (with FF = 83.46, J_{SC} = 24.90 mA cm^{-2} and V_{OC} = 1.15 V; Supplementary Fig. 43). A voltage loss of 0.38 V is the lowest documented for a NiO_x-based PSC (bandgap from the external quantum efficiency, Supplementary Fig. 42)[49].

We focused on improving the performance of the NiO_x-HTL inverted PSCs because they have shown high stability at elevated temperatures[19,49,50]. However, 2D treatments have been shown to be unstable above 50 °C, degrading in a matter of hours[51]; thus it was crucial to ascertain whether or not any new 2D treatment could withstand high temperatures. We prepared 2D- and quasi-2D-treated films and heated them at 65 °C for 20 h, periodically measuring their characteristics via TA spectroscopy (Supplementary Fig. 41). We found that the n distribution of both treatments was robust under heating, suggesting that the quasi-2D treatment could be used to produce extremely stable devices.

We evaluated the stability of the devices under accelerated-ageing conditions according to International Summit on Organic Photovoltaic Stability (ISOS) protocols[52]. We tracked the maximum power point (MPP) of two quasi-2D-treated devices under illumination at ~50% relative humidity. An unencapsulated device was monitored at room temperature for 1,000 h (ISOS-L-1I) and an encapsulated device on a temperature-controllable stage was monitored at 65 °C for 500 h (ISOS-L-3), and the results are shown in Fig. 5e,f, respectively. The unencapsulated room-temperature devices showed no degradation after 1,000 h of MPP tracking (4.9% increase in PCE), whereas the device baked at 65 °C lost around 8% of its maximum PCE after 500 h. On the basis of a linear extrapolation from these data, we estimate the T_{80} lifetime of this device (that is, the time required to drop to 80% of the initial efficiency) to be 1,190 h (Supplementary Fig. 45)[20,52]. After 500 h the MPP tracking for the heated device was paused but the cell remained under illumination at 65 °C, and after 12 h the MPP tracking was resumed. The PCE of the device recovered to 99% of the initial PCE, which is an encouraging indicator of its real-world long-term stability[53]. We note that the device structure was not altered for stability testing and the initial efficiency of both devices was >23% (Supplementary Fig. 44). Therefore, we report an ISOS-L-3 accelerated-ageing test that corresponds directly to high-efficiency PSCs (>20% PCE).

Conclusion

We presented a simple technique that alters the QW widths in 2D/3D perovskite heterostructures. This was tailored to improve inverted PSCs, and was accomplished by reducing the confinement within the 2D capping layer to reduce the electron barrier between the 3D and 2D perovskite species. This resulted in highly stable NiO_x-based PSCs with certified efficiency values, and could be useful in other metal halide-based optoelectronics devices in which well-passivated, negative–intrinsic contacts are desirable.

Online content

Any methods, additional references, Nature Research reporting summaries, source data, extended data, supplementary information, acknowledgements, peer review information; details of author contributions and competing interests; and statements of data and code availability are available at https://doi.org/10.1038/s41566-022-00985-1.

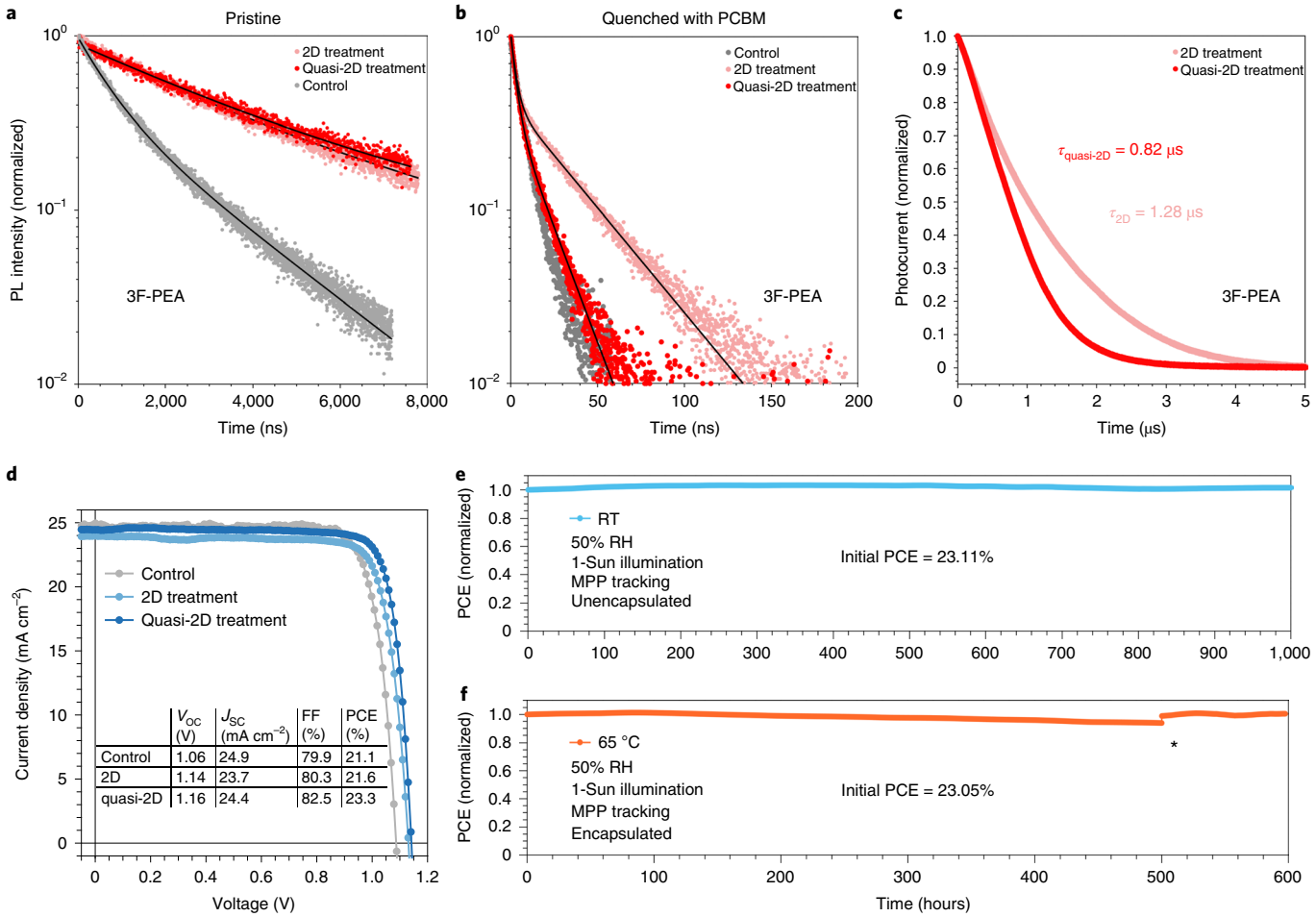

Fig. 5 | Carrier extraction and performance of quasi-2D-treated PSCs. a, Transient PL from bare films treated with 3F-PEA. **b**, The same films with PCBM as an electron quencher. **c**, Transient photocurrent measurements for devices using 3F-PEA-treated films. **d**, *J*–*V* curves from control, 2D- and quasi-2D-treated devices. Figures of merit are averages from 20 control, 2D- and quasi-2D-treated devices using 3F-PEA ligands. Statistics for devices using PEA and BTA ligands are also shown in Supplementary Figs. 33–36. **e**, Room-temperature (RT) MPP tracking of an unencapsulated device under 1-Sun illumination and 50% relative humidity (RH). **f**, MPP tracking of an encapsulated device held at 65 °C under 1-Sun illumination and 50% relative humidity (ISOS-L3 conditions). The asterisk indicates the point at which the MPP tracking was paused for 12 h.

Received: 13 July 2021; Accepted: 21 February 2022;
Published online: 07 April 2022

References

1. Yuan, M. et al. Perovskite energy funnels for efficient light-emitting diodes. *Nat. Nanotechnol.* **11**, 872–877 (2016).
2. Wei, M. et al. Ultrafast narrowband exciton routing within layered perovskite nanoplatelets enables low-loss luminescent solar concentrators. *Nat. Energy* **4**, 197–205 (2019).
3. Proppe, A. H. et al. Synthetic control over quantum well width distribution and carrier migration in low-dimensional perovskite photovoltaics. *J. Am. Chem. Soc.* **140**, 2890–2896 (2018).
4. Quan, L. N. et al. Ligand-stabilized reduced-dimensionality perovskites. *J. Am. Chem. Soc.* **138**, 2649–2655 (2016).
5. Jung, E. H. et al. Efficient, stable and scalable perovskite solar cells using poly(3-hexylthiophene). *Nature* **567**, 511–515 (2019).
6. Min, H. et al. Efficient, stable solar cells by using inherent bandgap of α-phase formamidinium lead iodide. *Science* **366**, 749–753 (2019).
7. Jeong, M. et al. Stable perovskite solar cells with efficiency exceeding 24.8% and 0.3-V voltage loss. *Science* **369**, 1615–1620 (2020).
8. Jiang, Q. et al. Surface passivation of perovskite film for efficient solar cells. *Nat. Photonics* **13**, 460–466 (2019).
9. Zhu, H. et al. Tailored amphiphilic molecular mitigators for stable perovskite solar cells with 23.5% efficiency. *Adv. Mater.* **32**, 1907757 (2020).
10. Liu, Y. et al. Ultrahydrophobic 3D/2D fluoroarene bilayer-based water-resistant perovskite solar cells with efficiencies exceeding 22%. *Sci. Adv.* **5**, eaaw2543 (2019).
11. Kim, G. et al. Impact of strain relaxation on performance of α-formamidinium lead iodide perovskite solar cells. *Science* **370**, 108–112 (2020).
12. Jeong, J. et al. Pseudo-halide anion engineering for α-$FAPbI_3$ perovskite solar cells. *Nature* **592**, 381–385 (2021).
13. Teale, S. et al. Dimensional mixing increases the efficiency of 2D/3D perovskite solar cells. *J. Phys. Chem. Lett.* **11**, 5115–5119 (2020).
14. Yoo, J. J. et al. An interface stabilized perovskite solar cell with high stabilized efficiency and low voltage loss. *Energy Environ. Sci.* **12**, 2192–2199 (2019).
15. Hu, Y. et al. Hybrid perovskite/perovskite heterojunction solar cells. *ACS Nano* **10**, 5999–6007 (2016).
16. Proppe, A. H. et al. Multication perovskite 2D/3D interfaces form via progressive dimensional reduction. *Nat. Commun.* **12**, 3472 (2021).
17. Jang, Y. W. et al. Intact 2D/3D halide junction perovskite solar cells via solid-phase in-plane growth. *Nat. Energy* **6**, 63–71 (2021).
18. Zhang, T. et al. Stable and efficient 3D-2D perovskite-perovskite planar heterojunction solar cell without organic hole transport layer. *Joule* **2**, 2706–2721 (2018).
19. Bai, S. et al. Planar perovskite solar cells with long-term stability using ionic liquid additives. *Nature* **571**, 245–250 (2019).
20. Lin, Y. H. et al. A piperidinium salt stabilizes efficient metal-halide perovskite solar cells. *Science* **369**, 96–102 (2020).
21. Zheng, X. et al. Managing grains and interfaces via ligand anchoring enables 22.3%-efficiency inverted perovskite solar cells. *Nat. Energy* **5**, 131–140 (2020).
22. Chen, S., Xiao, X., Gu, H. & Huang, J. Iodine reduction for reproducible and high-performance perovskite solar cells and modules. *Sci. Adv.* **7**, eabe8130 (2021).

23. Chen, C. et al. Arylammonium-assisted reduction of the open-circuit voltage deficit in wide-bandgap perovskite solar cells: the role of suppressed ion migration. *ACS Energy Lett.* **5**, 2560–2568 (2020).
24. Bai, Y. et al. Dimensional engineering of a graded 3D–2D halide perovskite interface enables ultrahigh V_{oc} enhanced stability in the p-i-n photovoltaics. *Adv. Energy Mater.* **7**, 1701038 (2017).
25. Park, S. M., Abtahi, A., Boehm, A. M. & Graham, K. R. Surface ligands for methylammonium lead iodide films: surface coverage, energetics, and photovoltaic performance. *ACS Energy Lett.* **5**, 799–806 (2020).
26. La-Placa, M. G. et al. Vacuum-deposited 2D/3D perovskite heterojunctions. *ACS Energy Lett.* **4**, 2893–2901 (2019).
27. Zhao, T., Chueh, C.-C., Chen, Q., Rajagopal, A. & Jen, A. K.-Y. Defect passivation of organic–inorganic hybrid perovskites by diammonium iodide toward high-performance photovoltaic devices. *ACS Energy Lett.* **1**, 757–763 (2016).
28. Proppe, A. H. et al. Photochemically cross-linked quantum well ligands for 2D/3D perovskite photovoltaics with improved photovoltage and stability. *J. Am. Chem. Soc.* **141**, 14180–14189 (2019).
29. Mahmud, M. A. et al. Double-sided surface passivation of 3D perovskite film for high-efficiency mixed-dimensional perovskite solar cells. *Adv. Funct. Mater.* **30**, 1907962 (2020).
30. Burgelman, M., Nollet, P. & Degrave, S. Modelling polycrystalline semiconductor solar cells. *Thin Solid Films* **361–362**, 527–532 (2000).
31. Zhou, L. et al. Highly efficient and stable planar perovskite solar cells with modulated diffusion passivation toward high power conversion efficiency and ultrahigh fill factor. *Sol. RRL* **3**, 1900293 (2019).
32. Cao, D. H., Stoumpos, C. C., Farha, O. K., Hupp, J. T. & Kanatzidis, M. G. 2D homologous perovskites as light-absorbing materials for solar cell applications. *J. Am. Chem. Soc.* **137**, 7843–7850 (2015).
33. Ma, J. & Wang, L. W. Nanoscale charge localization induced by random orientations of organic molecules in hybrid perovskite $CH_3NH_3PbI_3$. *Nano Lett.* **15**, 248–253 (2015).
34. Quintero-Bermudez, R. et al. Compositional and orientational control in metal halide perovskites of reduced dimensionality. *Nat. Mater.* **17**, 900–907 (2018).
35. Hu, J. et al. Synthetic control over orientational degeneracy of spacer cations enhances solar cell efficiency in two-dimensional perovskites. *Nat. Commun.* **10**, 1276 (2019).
36. Niu, T. et al. Interfacial engineering at the 2D/3D heterojunction for high-performance perovskite solar cells. *Nano Lett.* **19**, 7181–7190 (2019).
37. Gharibzadeh, S. et al. Record open-circuit voltage wide-bandgap perovskite solar cells utilizing 2D/3D perovskite heterostructure. *Adv. Energy Mater.* **9**, 1803699 (2019).
38. Briggs, D. & Seah, M. P. (eds) *Practical Surface Analysis. Auger and X-ray Photoelectron Spectroscopy* 2nd edn, Vol. 1 (Wiley, 1990).
39. Boehm, A. M., Liu, T., Park, S. M., Abtahi, A. & Graham, K. R. Influence of surface ligands on energetics at $FASnI_3/C_{60}$ interfaces and their impact on photovoltaic performance. *ACS Appl. Mater. Interfaces* **12**, 5209–5218 (2020).
40. Yoshida, H. Near-ultraviolet inverse photoemission spectroscopy using ultra-low energy electrons. *Chem. Phys. Lett.* **539–540**, 180–185 (2012).
41. Boehm, A. M., Wieser, J., Butrouna, K. & Graham, K. R. A new photon source for ultraviolet photoelectron spectroscopy of organic and other damage-prone materials. *Org. Electron.* **41**, 9–16 (2017).
42. Endres, J. et al. Valence and conduction band densities of states of metal halide perovskites: a combined experimental–theoretical study. *J. Phys. Chem. Lett.* **7**, 2722–2729 (2016).
43. She, X. J. et al. A solvent-based surface cleaning and passivation technique for suppressing ionic defects in high-mobility perovskite field-effect transistors. *Nat. Electron.* **3**, 694–703 (2020).
44. Kirchartz, T., Márquez, J. A., Stolterfoht, M. & Unold, T. Photoluminescence-based characterization of halide perovskites for photovoltaics. *Adv. Energy Mater.* **10**, 1904134 (2020).
45. Zhou, M., Sarmiento, J. S., Fei, C. & Wang, H. Charge transfer and diffusion at the perovskite/PCBM interface probed by transient absorption and reflection. *J. Phys. Chem. C* **123**, 22095–22103 (2019).
46. Proppe, A. H. et al. Spectrally resolved ultrafast exciton transfer in mixed perovskite quantum wells. *J. Phys. Chem. Lett.* **10**, 419–426 (2019).
47. Shao, Y., Yuan, Y. & Huang, J. Correlation of energy disorder and open-circuit voltage in hybrid perovskite solar cells. *Nat. Energy* **1**, 15001 (2016).
48. Chen, W. et al. Efficient and stable large-area perovskite solar cells with inorganic charge extraction layers. *Science* **350**, 944–948 (2015).
49. Ma, F. et al. Nickel oxide for inverted structure perovskite solar cells. *J. Energy Chem.* **52**, 393–411 (2020).
50. Boyd, C. C. et al. Overcoming redox reactions at perovskite–nickel oxide interfaces to boost voltages in perovskite solar cells. *Joule* **4**, 1759–1775 (2020).
51. Sutanto, A. A. et al. Dynamical evolution of the 2D/3D interface: a hidden driver behind perovskite solar cell instability. *J. Mater. Chem. A* **8**, 2343–2348 (2020).
52. Khenkin, M. V. et al. Consensus statement for stability assessment and reporting for perovskite photovoltaics based on ISOS procedures. *Nat. Energy* **5**, 35–49 (2020).
53. Lu, H. et al. Vapor-assisted deposition of highly efficient, stable black-phase $FAPbI_3$ perovskite solar cells. *Science* **370**, eabb8985 (2020).

Methods

Materials. All the materials were used as received without purification. Commercial indium tin oxide (ITO) substrates (20 Ω per square) with dimensions of 25 × 25 mm were purchased from TFD. PbI_2 and bathocuproine (BCP) were purchased from TCI. Caesium iodide (CsI) (99.999%) and fullerene (C_{60}) (99.5%) were purchased from Sigma-Aldrich. PEAI, FAI (formamidinium iodide) and MAI were purchased from GreatCell Solar. 2F-PEAI (2-fluoro-phenethylammonium iodide), 3F-PEAI, 4F-PEAI (4-fluoro-phenethylammonium iodide) and 1-naphthylmethylammonium iodide were purchased from Xi'an Polymer Light Technology. PCBM was purchased from Nano-C. All the solvents used in the process were anhydrous and purchased from Sigma-Aldrich.

Nickel oxide nanoparticle synthesis. The NiO_x nanoparticles were prepared via the hydrolysis of nickel nitrate following previous work[54,55]. Briefly, $Ni(NO_3)_2{\cdot}6H_2O$ (20 mmol) was dissolved in deionized water (20 ml) to obtain a dark-green solution. Then, NaOH aqueous solution (4 ml, 10 mol l^{-1}) was slowly added to the dark-green solution with stirring. After being stirred for 20 min, the colloidal precipitate was washed thoroughly using deionized water three times and dried at 80 °C for 6 h. The obtained green powder was then calcined at 270 °C for 2 h to obtain a black powder. The NiO_x nanoparticle ink was prepared by dispersing the obtained NiO_x nanoparticles in a mixed solution of deionized water and IPA (3:1, v/v) for a concentration of 10 mg ml^{-1}.

Solar cell fabrication. ITO glass was cleaned through sequential washing with detergent, deionized water, acetone and IPA. Before use, the ITO was cleaned with ultraviolet ozone for 20 min.

For the inverted solar cells, the substrate was spin-coated with a thin layer of NiO_x nanoparticle film using the NiO_x nanoparticle ink at 2,000 r.p.m. for 30 s. The perovskite absorber layers were deposited inside a nitrogen-filled glovebox with a controlled water and oxygen level of less than 1 ppm. The temperature inside was monitored to be 25–30 °C. The precursors for the $Cs_{0.05}FA_{0.85}MA_{0.1}PbI_3$ perovskites were prepared by dissolving the PbI_2, MAI, CsI and FAI in a mixed solvent (4:1 in volume) of DMF and dimethyl sulfoxide (DMSO), respectively. This was done by adding the powders to a vial (20 ml size) and then adding the mixed solvent (1 ml) before leaving the vial on a stirring hotplate set to 60 °C for 30 min; all steps were undertaken in a glovebox. For fabrication of the perovskite film, the substrate was spun at 2,000 r.p.m. for 30 s with an initial acceleration of 1,000 r.p.m., and then at 6000 r.p.m. for 10 s with an acceleration of 6000 r.p.m. per second. In the second step, anisole (150 µl) was added dropwise onto the substrate during the last 5 s of spinning. The substrate was immediately placed on a hotplate and annealed at 100 °C for 10 min. For the surface treatment, the 2D solutions were prepared by dissolving the 2D ligand salts (that is, PEAI, BTAI, 3F-PEAI, HAI and OTAI) with or without MAI and DMF in IPA. The ligand salt (1 mg ml^{-1}), MAI (0.5 mg ml^{-1}) and an IPA:DMF v/v ratio of 1:200 was used, unless stated otherwise. The 2D layer was fabricated by depositing the 2D ligand solution (150 µl) onto the perovskite film surface, and immediately after deposition the film was spun at a rate of 4,000 r.p.m. for 30 s with a 4,000 r.p.m. per second acceleration. The film was then annealed at 100 °C for 5 min.

For the ETL, either C_{60}/ALD-SnO_2 or PCBM/BCP were used. C_{60} was formed via evaporation, and deposition of the ALD-SnO_2 (atomic-layer-deposited tin(IV) oxide) was carried out using a PICOSUN R-200 Advanced ALD system. Water and tetrakis(dimethylamino)tin(IV) (TDMASn) were used as the oxygen and tin precursors, respectively. The precursor and substrate temperature was set to 75 °C and 85 °C, respectively. Nitrogen gas (90 sccm) was used as carrier gas. Pulse and purge times for water were 1 s and 5 s, respectively, and 1.6 s and 5 s, respectively, for TDMASn. The total deposition cycle is 134 s, corresponding to 20 nm of SnO_2.

PCBM was formed by spin coating the PCBM solution (20 mg ml^{-1} in chlorobenzene) at 1,000 r.p.m. for 30 s and then annealing at 100 °C for 5 min. Then a thin and uniform BCP layer was deposited via drop-casting 2–3 drops of BCP dissolved in IPA while spinning the substrate at 5,000 r.p.m. Finally, a 120-nm-thick silver contact was deposited on top of the BCP using thermal evaporation under high vacuum (<5 × 10^{-7} torr) using an Angstrom Engineering deposition system to produce a cell with an active area of 0.053 cm^2.

For non-inverted solar cells, the substrate was spin-coated with a thin layer of SnO_2 nanoparticle solution (1:3:3, SnO_2 (15% in water):IPA:water) at 3,000 r.p.m. for 20 s and annealed in ambient air at 150 °C for 1 h. The perovskite solution was prepared by dissolving $FAPbI_3$ (889 mg ml^{-1}), $MAPbBr_3$ (33 mg ml^{-1}) and MACl (33 mg ml^{-1}) in DMF/DMSO (8:1 v/v) mixed solvent. Then, the solution was coated onto the ITO/SnO_2 substrate through two consecutive spin-coating steps, at 1,000 r.p.m. for 5 s and 2,500 r.p.m. for 20 s. During the second spin-coating (2,500 r.p.m.) step, diethyl ether (1 ml) was poured onto the substrate after 15 s. The intermediate phase substrate was then put on a hotplate at 150 °C for 10 min. After the fabrication of the 3D perovskite film, the 2D layer was fabricated by depositing a solution (5 mg ml^{-1}) of PEAI in IPA onto the perovskite film and then spinning the substrate at 4,000 r.p.m. for 30 s. Then, the substrate was heat-treated at 100 °C for 5 min. For deposition of the hole transport material, a spiro-OMeTAD solution in chlorobenzene (90.9 mg mL^{-1}) was prepared, and lithium-bis(trifluoromethanesulfonyl) imide solution in acetonitrile (23 µl, 540 mg mL^{-1}) and pure 4-*tert*-butylpyridine (39 µl) were added to an aliquot of the solution (1.1 ml). The spiro-OMeTAD solution including additives was spin-coated onto the perovskite surface at 1,750 r.p.m. for 30 s. Finally, a gold electrode was deposited via thermal evaporation to produce a cell with an active area of 0.053 cm^2.

Reduced-dimensional film fabrication. Reduced-dimensional $(PEA)_2(MA/FA/Cs)_{n-1}Pb_nI_{3n+1}$ perovskite solutions were prepared by dissolving the appropriate stoichiometric quantities of PbI_2, MAI (or FAI or CsI) with PEAI in DMF/DMSO (4:1 v/v). The resulting solution was filtered using a polytetrafluoroethylene syringe filter (0.2 µm) before deposition. Then, the solution was coated onto the glass substrate through two consecutive spin-coating steps, at 1,000 r.p.m. for 5 s and 2,500 r.p.m. for 20 s. During the second spin-coating (2,500 r.p.m.) step, diethyl ether (1 ml) was poured onto the substrate after 15 s. The intermediate phase substrate was then put on a hotplate at 150 °C for 10 min.

Device testing. The current density–voltage (J–V) characteristics were measured using a Keithley 2400 source meter under illumination from a solar simulator (Class A, Newport) with a light intensity of 100 mW cm^{-2} (checked using a calibrated reference solar cell from Newport). The J–V curves were measured in a nitrogen atmosphere with a scanning rate of 100 mV s^{-1} (a voltage step of 10 mV and a delay time of 200 ms). The active area was determined by the aperture shade mask (0.049 cm^2 for small-area devices) placed in front of the solar cell. A spectral mismatch factor of unity was used for all J–V measurements. For stabilized output measurements at the MPP, the device testing chamber was left under ambient conditions. Solar cells were fixed at the MPP voltage, (determined from J–V sweeps in both scanning directions) and the current output was tracked over time.

Stability testing. Devices were placed in a homemade stability-tracking station. The illumination source is a white-light LED with its intensity calibrated to match 1-Sun conditions. For room-temperature tests (ISOS-L-1I), the device chamber was sealed and supplied with continuous nitrogen purging. For the ISOS-L-3 ageing test, the device chamber was left open in a room with 50 ± 10% relative humidity, and the solar cell was mounted on a metal plate kept at 65 °C using a heating element. A thermal couple attached to the metal plate was used to monitor and provide feedback control to the heating element to ensure temperature consistency. The MPP was tracked using a perturb-and-observe algorithm that updates the MPP value every 10 s. Encapsulation was done by capping the device with a glass slide, using UV-adhesive (LT-U001, Lumtec) as the sealant.

X-ray diffraction. X-ray diffraction patterns were collected using a Rigaku D/Max-2500 diffractometer equipped with Cu Kα1 radiation (λ = 1.54056 Å).

Grazing incidence wide-angle X-ray scattering. GIWAXS measurements were conducted at the BL14B1 beamline of the Shanghai Synchrotron Radiation Facility using X-rays with a wavelength of λ = 1.24 Å at a grazing incidence angle of 0.3° and an exposure time of 80 s. The GIXRD patterns were collected using a MarCCD 225 detector with a sample–detector distance of 280 mm and were presented in q coordinates using the equation $q = 4\pi\sin\theta/\lambda$, where θ is half of the diffraction angle. In the present GIXRD data, q has been calibrated by measuring the X-ray diffraction from a lanthanum hexaboride reference sample. Images were calibrated using lanthanum hexaboride and processed using the *Nika* software package[56] and the *GIXSGUI* MATLAB plug-in[57].

Simulations. Simulations of PSCs were conducted using the heterojunction solar cell simulator SCAPS-1D, version 3.3.07[30]. Full simulation details can be found in Supplementary Text 2.

Conductive atomic force microscopy. Scanning probe microscopy experiments were carried out under ambient conditions using an Asylum Research Cypher S AFM instrument with low-force-constant (k = 2.8 N m^{-1}), Ti/Ir-coated, silicon cantilevers (ASYELEC.01-R2). Contact-mode AFM was used to simultaneously produce surface and current maps applying a fixed bias voltage of −0.6 V. Measurements were obtained under top illumination from a 3 W white LED.

Transient absorption spectroscopy. Femtosecond laser pulses of 1,030 nm generated using a Yb:KGW laser at a 5 kHz repetition rate (Pharos, Light Conversion) were passed through an optical parametric amplifier (Orpheus, Light Conversion) to select 450 nm light. This served as the pump pulse, whereas the probe pulse was generated by focusing the initial 1,030 nm pulse into a sapphire crystal, which resulted in a white-light continuum (Helios, Ultrafast). With a temporal resolution of the system of ~350 fs, each time step meant delaying the probe pulse with respect to the pump, with time steps that increased exponentially. Every other pump pulse was blocked using a chopper to determine the change in optical density. After going through a grating spectrograph, the pulses were measured using a charge-coupled device (CCD) (Helios, Ultrafast).

Spinning in situ TA spectroscopy was performed using a purpose-built spinner, designed such that the incident probe light could pass through the spinning substrate and be directed into the CCD. The pump–probe delay was set to 1 ps. The time resolution of the system was 0.3 s. The measurements were taken in an ambient atmosphere with 35% relative humidity.

Photoluminescence quantum yield measurements. The excitation source was an unfocused beam from a 442 nm continuous-wave diode laser. Photoluminescence was collected using an integrating sphere with a pre-calibrated fibre coupled to a spectrometer (QE Pro, Ocean Optics) with an intensity of ~100 mW cm^{-2}. PLQY values were calculated using PLQY $= \frac{P_S}{P_{ex} \times A}$, where $A = 1 - P_L/P_{Ex}$, P_S is the integrated photon count of the sample emission on laser excitation, P_{ex} is the integrated photon count of the excitation laser when the sample is removed from the integrating sphere and P_L is the integrated photon count of excitation laser when sample is mounted in the integrating sphere and hit by the beam.

Space-charge-limited current measurements. SCLC measurements were obtained using electron-only (ITO/SnO_x/perovskite/PCBM/Ag) devices and hole-only (ITO/NiO_x/perovskite/poly(triaryl amine)/Au) devices separately. A Keithly 2400 source meter was used to measure the relevant J–V curves. We calculated the trap density (n_t) by SCLC measurement in the hole-only and electron-only devices. The trap-state density n_t can be calculated using the following relation:

$$n_t = \frac{V_{TFL}\varepsilon\varepsilon_0}{eL^2}$$

where e is the elementary charge, L is the perovskite film thickness (~650 nm), ε_0 is the vacuum permittivity, ε is the relative dielectric constant and V_{TFL} is the onset voltage of trap-filled limit region.

Transient photoluminescence spectroscopy. TRPL measurements were carried out using a Horiba Fluorolog time-correlated single photon counting system with photomultiplier tube detectors. A pulsed laser diode (634 nm, 110–140 ps pulse width) was used as the excitation source for steady-state and transient measurements. For transient measurements, a 7,200 ns period for unquenched films and an 800 ns period for quenched films (0.28 nJ per pulse) was used to capture accurate carrier lifetimes.

Inverse photoelectron spectroscopy and ultraviolet photoelectron spectroscopy. For combined UPS and IPES measurements, an Excitech H Lyman-α photon source (10.2 eV) with an oxygen-filled beam path was used for excitation, coupled with a PHI 5600 ultrahigh vacuum system with a hemispherical electron energy analyser. A sample bias of –5 V and a pass energy of 5.85 eV were used for UPS acquisition. IPES measurements were performed in the Bremsstrahlung isochromat mode with electron kinetic energies below 5 eV and an emission current of 2 μA to minimize sample damage. A Kimball Physics ELG-2 electron gun with a barium oxide cathode was used to generate the electron beam; the emitted photons were collected using a bandpass photon detector that included an optical bandpass filter (280 nm for 3F-PEA- and BTA-treated films, and 254 nm for the control and PEA-treated films) and a photomultiplier tube (R585, Hamamatsu Photonics). Samples were held at a −20 V bias during all IPES measurements and the ultrahigh vacuum chamber was blacked-out to exclude external light.

Perovskite films sent for combined UPS/IPES were fabricated on ITO/NiO_x substrates.

UPS measurements of quasi-2D perovskite films were carried out using a Thermo Fisher ESCALAB 250XL instrument; a −10 V bias was applied for UPS measurements.

Transient photovoltage/photocurrent measurements. These measurements were carried out according to ref. [47].

Kelvin probe force microscopy. KPFM was conducted using an MFP-3D AFM (Asylum Research, Oxford Instruments) with conductive Ti/Ir-coated tips (ASYELEC.01-R2 probe, f=71.72 kHz, k=2.8 N m^{-1}). The tips were calibrated using Sader's method[58,59]. The KPFM measurement was implemented using a two-path method at a scan rate of 0.5 Hz, where the first pass in every scan line was used to determine the topography and the following second pass was used to measure the contact potential difference between the tip and the sample. The second pass was scanned by raising the tip at a fixed 20 nm height above the sample following the topography. Each set of samples was arranged in proximity on a common substrate and were measured using the same tip and scanning parameters. We also adopted different scanning sequences of the samples in each set to ensure that the obtained potential trend is reliable and the global drift (if any) is not dominating. The two sets of samples (PEA- and 3F-PEA-treated) were measured using different probes, thus a shift in the overall potential is observed.

Reporting Summary. Further information on research design is available in the Nature Research Reporting Summary linked to this article.

Data availability

Source data are provided with this paper. All the data supporting the findings of this study are available within this article and its Supplementary Information. Any additional information can be obtained from corresponding authors upon request.

References

54. Chen, H. et al. Efficient and stable inverted perovskite solar cells incorporating secondary amines. *Adv. Mater.* **31**, 1903559 (2019).
55. Chen, H. et al. Band alignment towards high-efficiency NiO_x-based Sn-Pb mixed perovskite solar cells. *Sci. China Mater.* **64**, 537–546 (2021).
56. Ilavsky, J. *Nika*: software for two-dimensional data reduction. *J. Appl. Crystallogr.* **45**, 324–328 (2012).
57. Jiang, Z. *GIXSGUI*: a MATLAB toolbox for grazing-incidence X-ray scattering data visualization and reduction, and indexing of buried three-dimensional periodic nanostructured films. *J. Appl. Crystallogr.* **48**, 917–926 (2015).
58. Sader, J. E. et al. Spring constant calibration of atomic force microscope cantilevers of arbitrary shape. *Rev. Sci. Instrum.* **83**, 103705 (2012).
59. Sader, J. E., Lu, J. & Mulvaney, P. Effect of cantilever geometry on the optical lever sensitivities and thermal noise method of the atomic force microscope. *Rev. Sci. Instrum.* **85**, 113702 (2014).

Acknowledgements

This research was made possible by the US Department of the Navy, Office of Naval Research Grant (N00014-20-1-2572). This work was supported in part by the Ontario Research Fund-Research Excellence program (ORF7-Ministry of Research and Innovation, Ontario Research Fund-Research Excellence Round 7). We appreciate the Shanghai Synchrotron Radiation Facility (beamline 14B and 16B) and X. Gao and Z. Su for their help with GIWAXS characterization. Z.N. is grateful for support by the National Key Research Program (2021YFA0715502, 2016YFA0204000) and the National Science Fund of China (61935016). S.M.P., H.R.A. and K.R.G. acknowledge the US Department of Energy under Grant DE-SC0018208 for supporting the UPS and IPES measurements. T.F. and T.C. acknowledge the Canadian Foundation for Innovation and the Natural Science and Engineering Council of Canada (NSERC) for KPFM measurements. F.L and Y.G. were funded by the King Abdullah University of Science and Technology (KAUST) Office of Sponsored Research (OSR) under Award No: OSR-CARF/CCF-3079 and OSR-2018-CRG7-3737.

Author contributions

H.C., S.T., B.C. and Y.H. conceived the idea. H.C., K.B., L.G. and S.T. prepared samples for characterization. S.M.P. and H.R.A. performed UPS and IPES measurements, and S.M.P., H.R.A., S.T. and K.R.G. analysed the data. S.T. performed the TA experiments and analysed the data with Y.G. and F.L. The in situ TA system for use in this paper was developed by S.T., A.K.J. and A.H.P. The in situ measurements were performed by S.T. who also analysed the data. T.Z. performed the DFT calculations and analysed the data. B.C. performed PLQY measurements and H.C. measured the PL lifetimes. M.W. carried out the transient photocurrent and photovoltage measurements and S.T. analysed the data. S.T. performed SCAPS simulations. S.T. collected the thin-film X-ray diffraction patterns. C.H. and D.Y. performed the GIWAXS experiments and obtained the SEM images. S.T. and B.C. analysed the data. The KPFM measurements were performed by T.C., and T.F. analysed the data. H.C. and W.Z. carried out the SCLC measurements and S.T. analysed the data. S.T. conducted the c-AFM measurements. H.C. fabricated all the devices for performance and certification, B.C. and S.H. helped with device certification. B.C. built the heated MPP-tracking station. Q.Z., K.X. and C.Z. carried out the UPS on bulk 2D films. Z.N. and E.H.S. supervised and funded the work. S.T. wrote the draft manuscript with input from B.C. and E.H.S. All authors contributed to the revision of the final paper.

Competing interests

The authors declare no competing interests.

Additional information

Supplementary information The online version contains supplementary material available at https://doi.org/10.1038/s41566-022-00985-1.

Correspondence and requests for materials should be addressed to Zhijun Ning or Edward H. Sargent.

Peer review information *Nature Photonics* thanks Mohammad Khaja Nazeeruddin, Ling Xu the other, anonymous, reviewer(s) for their contribution to the peer review of this work.

nature research

Corresponding author(s): Prof. Edward Sargent, Prof. Zhijun Ning

Solar Cells Reporting Summary

Nature Research wishes to improve the reproducibility of the work that we publish. This form is intended for publication with all accepted papers reporting the characterization of photovoltaic devices and provides structure for consistency and transparency in reporting. Some list items might not apply to an individual manuscript, but all fields must be completed for clarity.

For further information on Nature Research policies, including our data availability policy, see Authors & Referees.

Experimental design

Please check: are the following details reported in the manuscript?

1. Dimensions			
Area of the tested solar cells	☒ Yes ☐ No	The small area of solar cells is 0.053 cm2 (Methods - Solar Cell fabrication)
Method used to determine the device area	☒ Yes ☐ No	The active area is 0.049 cm2 (Methods - Device testing)
2. Current-voltage characterization			
Current density-voltage (J-V) plots in both forward and backward direction	☒ Yes ☐ No	Figure S46
Voltage scan conditions *For instance: scan direction, speed, dwell times*	☒ Yes ☐ No	JV curves were measured with a scanning rate of 100 mV/s (voltage step of 10mV and delay time of 200ms) (Methods - Device testing)
Test environment *For instance: characterization temperature, in air or in glove box*	☒ Yes ☐ No	Unencapsulated devices were tested in a nitrogen environment. Encapsulated devices were tested at 65 degrees Celsius in 50% relative humidity. (Figure 5e,f, Methods - Stability testing)
Protocol for preconditioning of the device before its characterization	☒ Yes ☐ No	No preconditioning was used
Stability of the J-V characteristic *Verified with time evolution of the maximum power point or with the photocurrent at maximum power point; see ref. 7 for details.*	☒ Yes ☐ No	Maximum power point tracking (Figure 5 e,f)
3. Hysteresis or any other unusual behaviour			
Description of the unusual behaviour observed during the characterization	☒ Yes ☐ No	Cells saw negligible hysteresis (~ 1%) (Fig. S46)
Related experimental data	☒ Yes ☐ No	Fig. S46
4. Efficiency			
External quantum efficiency (EQE) or incident photons to current efficiency (IPCE)	☒ Yes ☐ No	Figure S42
A comparison between the integrated response under the standard reference spectrum and the response measure under the simulator	☒ Yes ☐ No	Figure S42
For tandem solar cells, the bias illumination and bias voltage used for each subcell	☐ Yes ☒ No	This report does not include tandem solar cells
5. Calibration			
Light source and reference cell or sensor used for the characterization	☒ Yes ☐ No	Newport, Class A simulator is used for the measurements (Methods, Device testing)
Confirmation that the reference cell was calibrated and certified	☒ Yes ☐ No	The light intensity was calibrated by reference solar cell by Newport (Methods - Device testing)

Calculation of spectral mismatch between the reference cell and the devices under test	☐ Yes ☒ No	We rely on certified efficiency results.

6. Mask/aperture

Size of the mask/aperture used during testing	☒ Yes ☐ No	0.049 cm2 (Methods - Device testing)
Variation of the measured short-circuit current density with the mask/aperture area	☐ Yes ☒ No	We did not evaluate multiple testing apertures

7. Performance certification

Identity of the independent certification laboratory that confirmed the photovoltaic performance	☒ Yes ☐ No	NREL (Figure S43)
A copy of any certificate(s) *Provide in Supplementary Information*	☒ Yes ☐ No	Figure S43

8. Statistics

Number of solar cells tested	☒ Yes ☐ No	Statistical analysis was performed on 10-20 devices of each architecture (Figure S33 - S39)
Statistical analysis of the device performance	☒ Yes ☐ No	Figure S33 - S39

9. Long-term stability analysis

Type of analysis, bias conditions and environmental conditions *For instance: illumination type, temperature, atmosphere humidity, encapsulation method, preconditioning temperature*	☒ Yes ☐ No	Stability tests were performed under 1-sun illumination from a white LED and MPP-tracked conditions. Unencapsulated devices were tested in a nitrogen environment. Encapsulated devices were tested at 65 degrees Celsius in 50% relative humidity. (Figure 5 e,f, Methods - Stability testing)